7

Waveform Analysis for Small-Footprint Pulsed Laser Systems

Uwe Stilla and Boris Jutzi

CONTENTS

7.1 Introduction 215
7.2 Characterization of a Laser System 217
7.2.1 Laser Type 217
7.2.2 Modulation Technique 218
7.2.3 Measurement Technique 218
7.2.4 Detection Technique 219
7.2.5 Multiphoton Detection 219
7.2.6 Single-Photon Detection 220
7.2.7 Construction 221
7.3 Modeling 221
7.3.1 Waveform of the Laser Pulse 221
7.3.2 Spatial Energy Distribution 222
7.4 Analyzing the Waveform 223
7.4.1 Peak Detection 224
7.4.2 Leading Edge Detection 224
7.4.3 Constant Fraction Detection 225
7.4.4 Center of Gravity Detection 225
7.4.5 Gaussian Decomposition 227
7.4.6 Deconvolution 227
7.5 Attribute Extraction 228
7.6 Summary and Outlook 232
References 233

7.1 Introduction

Aerial photogrammetry and airborne laser scanning (ALS) are the two most widely used methods for generating digital elevation models (DEMs), including digital terrain models (DTMs) that depict ground topography and digital surface models (DSMs) that depict the height of the ground, structures, and vegetation cover. In photogrammetry, the distance to a spatial surface is classically derived from a triangulation of corresponding image points from two or more overlapping images of the surface. These points are chosen manually or

detected automatically by analyzing image structures. In contrast to photogrammetry, active laser scanner systems allow a direct and illumination-independent measurement of the distance to a surface, otherwise known as the range.

The interrelationship between aerial photogrammetry and ALS has been intensely discussed within the aerial surveying community in the last decade. Different comparison factors concerning data acquisition (e.g., coverage, weather conditions, costs, etc.) and surface reconstruction (e.g., accuracy, redundancy, post-processing time, etc.) have to be taken into account to choose the optimal method for a certain mapping campaign. An example of a study comparing photogrammetric image matching versus laser scanning for generation of high-quality DEMs for glacier monitoring is given in Wuerlaender et al. (2004). In contrast to a decision to use one or the other technique, in some fields of applications a combined processing of laser data and stereo images is advantageous as shown in the generation of the extraterrestrial DTMs of Mars (Albertz et al., 2005; Spiegel et al., 2006) or DSMs for building characterization.

Conventional pulsed laser scanner systems for topographic mapping are based on time-of-flight ranging techniques to determine the range to the illuminated object. The time-of-flight is measured by the elapsed time between the emitted and backscattered laser pulses. The signal analysis to determine this time typically operates with analog threshold detection. For targets that have surfaces at different ranges illuminated by a single laser pulse, more than one backscattered pulse may be detected per emitted pulse. Most ALS systems are able to capture, at a minimum, the range for the first- and last-detected backscattered pulses. Some systems acquire ranges up to as many as five per emitted pulse for multiple backscattered pulses. First-pulse detection is the optimal choice to measure the hull of partially penetrable objects or the so-called volume scattering targets (e.g., canopy of trees). Last-pulse detection should be chosen to measure nonpenetrable surfaces (e.g., ground surfaces).

Currently, some commercial ALS systems not only capture the range for multiple pulse reflections but also digitize and record the received signal of the reflected laser energy, which allows for the so-called full-waveform analysis. This offers the possibility of analyzing the waveform off-line using digital signal processing methods in order to extract different surface attributes from the received signal based on the shape of the return pulses.

In the last decade, some waveform analysis investigations were carried out to explore the structure of vegetation and estimate aboveground biomass. For example, NASA developed the waveform-recording laser vegetation imaging sensor (LVIS) to measure vertical density profiles in forests (Blair et al., 1999). This experimental airborne system operates at altitudes up to 10 km and acquires waveforms for large diameter laser footprints (nominally 20 m) acquired across a wide swath. Another NASA system operating with a large footprint is the spaceborne geoscience laser altimeter system (GLAS) mounted on the ice, cloud, and land elevation satellite (ICESat). GLAS measures height distributions of atmospheric clouds and aerosols, and surface elevations of ice sheets, land topography, and vegetation (Brenner et al., 2003; Zwally et al., 2002). It is a profiling system that operates with a footprint diameter of 70 m and measures elevation changes with decimeter accuracy (Abshire et al., 2005; Schutz et al., 2005). In the analysis of data from both systems, surface characteristics are determined by comparing a parametric description of the transmitted and received waveforms (Hofton et al., 2000; Harding and Carabajal, 2005). Because the laser footprint is large and illuminates multiple surfaces, the resulting return waveform is an integrated, spatially nonexplicit representation of the range to illuminated surfaces separated both vertically and horizontally. The geometric organization of surfaces within a single footprint can therefore not be determined.

AQ1

In contrast to large-footprint systems, small-footprint ALS systems illuminate only one or a few surfaces within the footprint, yielding waveforms with distinct return pulses corresponding to specific surfaces. One of the first developed small-footprint waveform-recording systems is the scanning hydrographic operational airborne lidar survey (SHOALS) instrument used for monitoring nearshore bathymetric environments. SHOALS has been in full operation since 1994 (Irish and Lillycrop, 1999; Irish et al., 2000). More recently commercial full-waveform ALS systems for terrestrial mapping have been developed (Jutzi and Stilla, 2006b; Wagner et al., 2006), which operate with a transmitted pulse width of 4–10 ns and allow digitization and acquisition of the waveform with approximately 0.5–1 GSample/s. Reitberger et al. (2006, 2007) have recently reported results that show clearly the potential of airborne, small-footprint, full-waveform data for the comprehensive analysis of tree structure and species classification. A set of key attributes have been defined and extracted based on the 3d distribution of the returns in combination with their characteristics in the full-waveform signal, providing information about tree microstructure such as the organization of the trunk and branches.

In this chapter, we focus on a given application in the context of a data set from a given sensor rather than on general principles. Specifically, we describe the different approaches for designing a laser system, modeling the spatial and temporal properties of the emitted lasers pulses, detecting return pulses, and deriving attributes from the waveform. We emphasize aspects of the received waveform that are especially relevant for the newly available small-footprint, full-waveform commercial systems that yield distinct return pulses when multiple surfaces are illuminated by a laser pulse.

The design of a laser system impacts its measurement capabilities and the manner in which the signal has to be modeled and analyzed. Section 7.2 gives a brief overview of the features that characterize the design of laser ranging systems. Section 7.3 focuses on modeling of the temporal waveform and the spatial beam distribution. Different strategies for pulse detection are explained in Section 7.4. Section 7.5 describes the attributes that can be extracted from a single laser shot and presents an analysis of an entire scene that was recorded with an experimental small-footprint, full-waveform laser ranging system. A summary and outlook is given in Section 7.6.

7.2 Characterization of a Laser System

Depending on the application, laser systems can be designed in different ways. They may differ in techniques concerning the type of laser used, the modulation, type of measured features, detection method, or design of beam paths (construction). Figure 7.1 sketches a simplified overview of features characterizing a laser system. More detailed descriptions can be found in Kamermann (1993).

7.2.1 Laser Type

A laser works as an oscillator and an amplifier for monochromatic radiation (infrared, visible light, or ultraviolet). The operative wavelength of available lasers is located between 0.1 µm und 3 mm. For comparison, it should be mentioned that the visible domain is from 0.37 to 0.75 µm. To achieve a good signal-to-noise ratio (SNR) over long ranges, conventional scanning laser systems emit radiation with high energy. However, this could endanger the health of humans due to the focusing of laser radiation on the retina, which is most

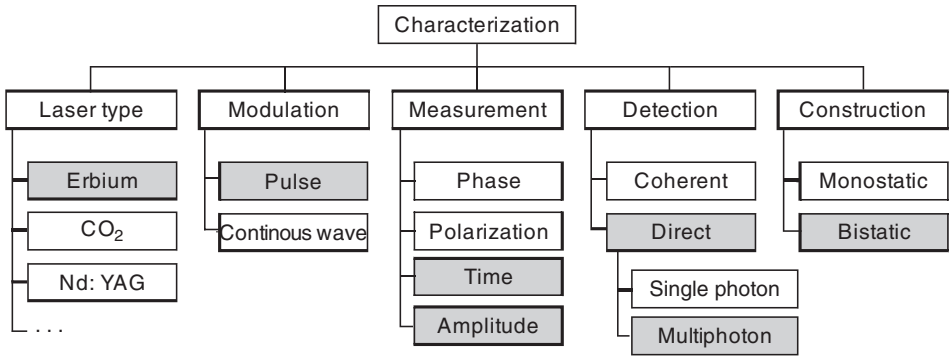

FIGURE 7.1
Features characterizing a laser system (with shaded boxes indicating the characteristics that are the focus of this chapter).

susceptible to damage at visible wavelengths. For this reason, most eye-safe laser systems used for mapping purposes operate with a wavelength outside the visible spectrum. This allows working with an emitted energy that is many times higher (up to 10^6) compared to the visible domain without the potential for retinal damage. Eye-safe lasers of greatest interest for long-range laser scanning are erbium-fiber lasers, carbon dioxide (CO_2) lasers, and neodymium:YAG (Nd:YAG) lasers.

Erbium-fiber lasers are optically pumped by a semiconductor diode and the active medium is an erbium-doped fiber. Their construction can be compact while still achieving a high output power. CO_2 lasers use carbon dioxide in gas form as the active medium. Although their construction is simple, their large size and mass are significant disadvantages. Solid-state Nd:YAG lasers can be pumped by various sources that define the characteristics of the emitted laser radiation. In this contribution we focus on erbium-fiber lasers (Figure 7.1).

7.2.2 Modulation Technique

Concerning modulation techniques, laser systems can be divided into two groups: continuous wave (cw) and pulsed lasers. A cw laser continuously emits electromagnetic radiation. The temporal energy distribution of the transmitted signal is influenced by amplitude modulation (AM) or frequency modulation (FM). Depending on the applied modulation technique, AQ3
specific measurement techniques (Section 7.2.3) are required. A pulsed laser emits electromagnetic radiation in pulses of short duration. For laser ranging it is desirable to emit a pulse as short as possible and with a pulse energy as high as possible in order to obtain a precise range with a high probability of detection. However, design limitations on maximum peak power introduce a trade-off that requires a compromise between the length and the energy of the pulse. The length of the pulse (full width at half maximum, FWHM) is typically between 2 and 10 ns. For applications in remote sensing with long ranges, pulsed lasers with higher power density as compared to cw lasers are advantageous. In this contribution we focus on pulsed laser systems (Figure 7.1).

7.2.3 Measurement Technique

Measurement techniques using laser systems can be distinguished by the exploited signal properties such as phase, amplitude, frequency, polarization, time, or any combination

of them. An amplitude modulated ~~(AM)~~ cw laser system is used to measure the range by exploiting the phase of a sinusoidal modulated signal. A phase difference Φ_d can be determined from a given phase of the transmitted signal and the measured phase of the received signal. With wavelength λ_m of the modulated signal, a corresponding range r can be calculated by $r = \lambda_m \cdot \Phi_d / 4\pi$. If the measurement of the phase difference Φ_d cannot be distinguished from $\Phi_d + n\pi$, the unambiguity interval of the range measurement will be limited to a maximum range $r_{max} = \lambda_m / 2$. Assuming that the system is able to resolve an angle difference $\Delta\Phi_d$, the range resolution Δr corresponds according to $\Delta r = \lambda_m \cdot \Delta\Phi_d / 4\pi$. To increase the range resolution for a given $\Delta\Phi_d$, the modulation wavelength λ_m has to be decreased. However, this results in a reduction of the unambiguity interval of the range determination.

The problem of ambiguity can be solved by using multiple simultaneous offset sinusoidal modulation frequencies (multiple-tone sinusoidal modulation). In this case the maximum modulation wavelength defines the unambiguity and the minimum modulation wavelength defines the range resolution. In addition to this, partially illuminated surfaces with different ranges within the beam corridor result in a superimposed signal depending on the range and the reflectance of the surface. Because only a single phase value can be determined at the receiver, the ambiguities caused by the partially illuminated surfaces cannot be resolved (Thiel and Wehr, 2004). An incorrect intermediate value is measured.

The measurement of the amplitude value is feasible for cw lasers as well as for pulsed lasers. The amplitude is influenced by background radiation, the range of the object to the laser system, and the size, reflectance, slope, and roughness of the illuminated surface. In this chapter, we are interested in measuring and analyzing the received pulse waveform, i.e., the dependence of the intensity over time (Figure 7.1).

7.2.4 Detection Technique

Detection techniques can be divided into coherent detection and direct detection (Jelalian, 1992). Coherent detection is based on signal amplification due to constructive interference of the wave front of the received signal with that of the reference signal emitted from a cw laser. In direct detection laser systems, the received optical energy is focused onto a photosensitive element that generates an output signal that depends on the received optical power. Two direct detection techniques are appropriate for recording the temporal characteristics of the backscattered signal: multiphoton detection and single-photon detection.

7.2.5 Multiphoton Detection

The classical measurement technique for direct detection operates with a photodiode. For optical detectors, a positive intrinsic negative diode (PIN) or the more sensitive avalanche photodiode (APD) is used. The photodiode generates an electrical signal (voltage or current) that is directly proportional to the optical power of incident light composed of multiple photons. Figure 7.2 sketches a pulse resulting from a varying number of photons n over time t. For a detailed analysis of the analog signal a digitizing receiver unit is essential. To analyze the signal of the emitted short duration laser pulse with only a few nanoseconds pulse width, a high bandwidth receiver that resolves the signal at gigahertz rates and a correspondingly high digitizer sampling rate is required. Increasing bandwidth results in decreasing sensitivity of the photodiode, which can be compensated by increasing the power of the emitting laser source. An example of an Nd:YAG laser pulse sampled with 5 GSample/s is given in Figure 7.4a.

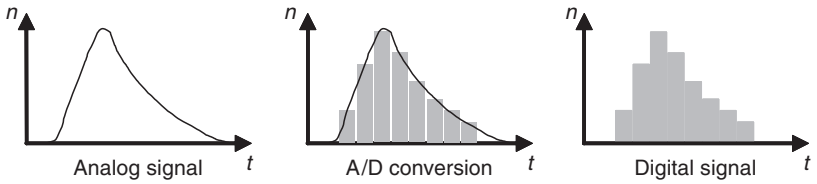

FIGURE 7.2
Digital recording of the signal with multiphoton detection.

7.2.6 Single-Photon Detection

The principle of single-photon detection is depicted in Figure 7.3. A short duration pulse is emitted by the laser source. A single photon of the backscattered pulse is detected by the receiver after time interval τ_1. This event blocks the receiver for a certain period of time during which no further photons are able to trigger the receiver. The time-of-flight of this single event is collected into a corresponding time bin of a histogram. After the period of blocking, the receiver is open to detect a new single-photon event. Multiple measurements are repeated and the time-of-flight of each single event ($\tau_2, \tau_3, \ldots$) is registered into the corresponding time bin of the histogram.

Let us assume a stationary scene and a stationary sensor platform. In this case, the statistical properties of the laser radiation do not change with the time and time-average quantities are equal to the ensemble quantities. Under these assumptions, the radiation ensembles are stationary and ergodic (Papoulis, 1984; Troup, 1972). The counting of single-photon events with assignment of their time-of-flight into time bins of a histogram is closely related to the integration of multiphotons over time (Alexander, 1997; Gagliardi and Karp, 1976; Loudon, 1973). In other words, the temporal waveform of the pulse can be reconstructed from a histogram of single-photon arrivals over time.

Many transmit pulses are necessary to obtain the waveform with single-photon detection. The quality of the sampled waveform depends on the number of photon counts. Various optical detectors can be used for this purpose, namely, PMT (photomultiplier tubes), MCP (microchannel plate), or APD detectors. Figure 7.4b shows a pulse plotted from a histogram containing the time-of-flight measurements from 16252 photons distributed in 50 bins, where the bin width is 40 ps. Note that the FWHM of the pulse

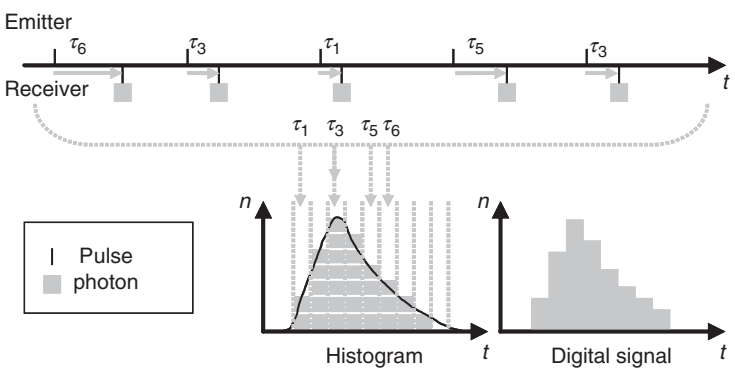

FIGURE 7.3
Digital recording of the signal with single-photon detection.

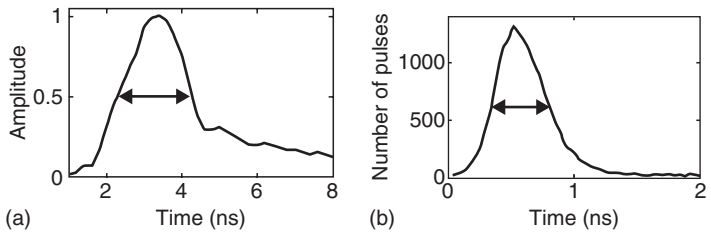

FIGURE 7.4
Examples for pulses backscattered from a diffuse surface. (a) Multiphoton detection (FWHM = 2.1 ns) and (b) single-photon detection (FWHM = 0.4 ns).

in Figure 7.4a is about five times of the pulse in Figure 7.4b. In this chapter, we focus on multiphoton detection (Figure 7.1).

7.2.7 Construction

Depending on the construction of the transmitter and receiver optics, monostatic and bistatic laser systems can be distinguished.

Monostatic laser systems have transmitter and receiver optics collocated on the same optical axis. A disadvantage of this construction is the higher number of components compared to a bistatic laser system, increasing the effort needed to optimally align the components. Advantages of this construction are the isogonal measurement of angles and the exact measurement of ranges, because the illuminated surface area and the observed field of view of the receiver are coincident for all ranges.

Bistatic laser systems have a transmitter and receiver optics that are spatially separated and thus the illumination and view angles are divergent. In general, both optics are close together and oriented in nearly the same direction. Objects are illuminated via a lens from the transmitter optic and the backscattered radiation is transferred via a separate lens to the receiver optic. An advantage of this measurement system is that the design can be easily constructed. A disadvantage of this design is that depending on the range to the illuminated surface the angle between the transmitter and the receiver optic varies. Furthermore, depending on the range, only a partial overlap is obtained between the illuminated surface and the observed field of view.

7.3 Modeling

The received waveform depends on the transmitted waveform of the emitted laser pulse, the spatial energy distribution of the beam, and the geometric and reflectance properties of the surface. In order to describe the temporal and spatial properties of a pulse, appropriate models that parameterize the pulse attributes have to be introduced.

7.3.1 Waveform of the Laser Pulse

Mathematical functions can be used to approximate the shape of laser pulse waveforms. Depending on the system, the shape may be best represented by a rectangular, exponential, or Gaussian distribution. A simple model is given by a rectangular distribution $s(t)$ with an amplitude a, pulse width w, and time delay τ

$$s(t) = a\,\mathrm{rect}\left\{-\frac{(t-\tau)}{w}\right\} = \begin{cases} a & \text{for} \quad -\tau \le t \le w-\tau \\ 0 & \text{else.} \end{cases} \tag{7.1}$$

Especially for short laser pulses a rectangular model often differs from the measured shape. A waveform with an exponential distribution (e.g., for a Q-switched laser) is applied by Steinvall (2000)

$$s(t) = t^2 \exp\left\{-\frac{(t-\tau)}{w}\right\} \tag{7.2}$$

A temporally symmetric Gaussian distribution for modeling the waveform of the spaceborne GLAS is proposed by Brenner et al. (2003). The basic waveform $s(t)$ of the used laser system can be described by

$$s(t) = \frac{2a}{w}\sqrt{\frac{\ln(2)}{\pi}}\exp\left\{-4\ln(2)\frac{(t-\tau)^2}{2w^2}\right\} \tag{7.3}$$

The width of a pulse w is commonly defined as one-half of the pulse's maximum amplitude known as FWHM.

7.3.2 Spatial Energy Distribution

The spatial energy distribution of a laser (also known as the beam profile) depends on the pump source, the optical resonator, and the laser medium. In general, beam profiles are modeled by a cylindrical distribution (top-hat form) or by a 2d-symmetric Gaussian distribution (Kamermann, 1993). The measured cylindrical beam distribution of a pulsed erbium fiber laser that operates at a wavelength of 1550 nm is depicted in Figure 7.5. A Gaussian

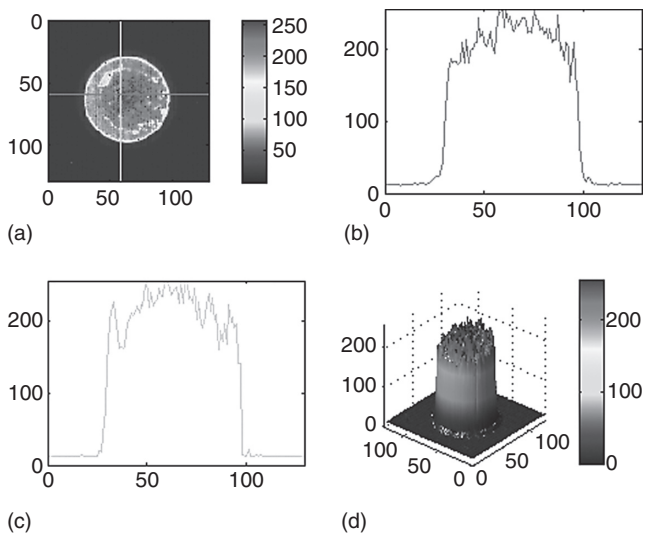

FIGURE 7.5
Measured cylindrical beam distribution (top-hat form). (a) 2d visualization, with the row (red) and column (green) of the maximum intensity indicated, (b) profile of the indicated row, (c) profile of the indicated column, and (d) 3d visualization.

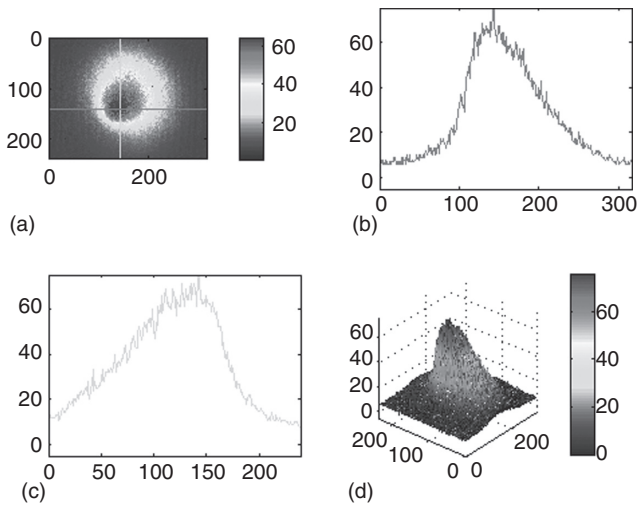

FIGURE 7.6
Measured Gaussian beam distribution. (a) 2d visualization, with the row (red) and column (green) of the maximum intensity indicated, (b) profile of the indicated row, (c) profile of the indicated column, and (d) 3d visualization.

beam distribution of a Raman shifted Nd:YAG laser that operates at a wavelength of 1543 nm is depicted in Figure 7.6. Both measurements differ more or less from these idealized distributions.

7.4 Analyzing the Waveform

Various detection methods are used to extract attributes of the reflecting surface from the waveform. To obtain the surface attributes, each waveform $s(t)$ is analyzed. The surface within the beam corridor generates a return pulse. To detect and separate this pulse from the noise, a signal-dependent threshold is estimated using the signal background noise. For example, in one particular implementation if the intensity of the waveform is above three times the noise standard deviation ($3\sigma_n$) for a duration of at least the full-width-half-maximum of the pulse, a pulse is assumed to be found. The section of the waveform including the detected pulse is passed onto the subsequent processing steps.

Typical surface attributes to extract from a waveform are range, elevation variation, and reflectance corresponding to the waveform attributes of time, width, and amplitude.

A rough surface, i.e., a surface of a certain vertical extent, will widen the laser pulse upon reflection. Therefore, the width of the pulse is a measure of the elevation variation of the surface. In addition, the widening of the pulse causes the reflected photons to be spread over a greater amount of time, thus reducing the peak amplitude. Therefore, to estimate the elevation variation or reflectance attributes of a surface, the pulse width and amplitude have to be known. Estimating just the amplitude of a pulse without considering this dependency will lead to inaccurate and noisy reflectance values. Determination of the range to a surface can be accomplished with different schemes that include peak detection, leading edge ranging, constant fraction detection, center

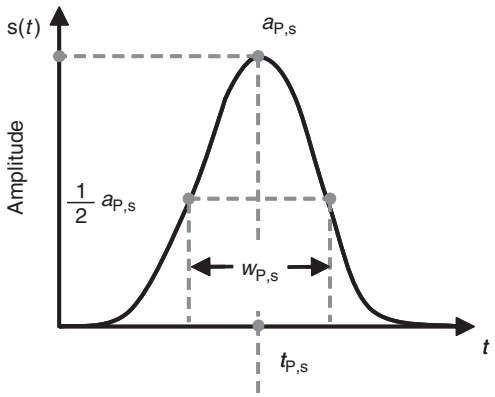

FIGURE 7.7
Attribute extraction with peak detection.

of gravity detection, and Gaussian decomposition and deconvolution. A discussion of key elements of each approach follows.

7.4.1 Peak Detection

The values of range $r_{P,s}$ and amplitude are determined at the maximum pulse amplitude $a_{P,s}$ (Figure 7.7), and the width $w_{P,s}$ is estimated at full-width-half-maximum of the pulse. Local spikes on the pulse waveform strongly effect the attribute extraction. Therefore, for noisy signals, a smoothing filter is recommended to determine the global maxima.

7.4.2 Leading Edge Detection

A threshold crossing of the pulse waveform leading edge determines the range value $r_{LE,s}$ (Figure 7.8). The threshold value can be a predefined fixed value, but then the ranging detection strongly depends on the amplitude and width of the pulse waveform, introducing a ranging bias dependent on pulse shape referred to as range walk. The half of the maximum amplitude $a_{LE,s}$ of the pulse for a threshold is used for range determination.

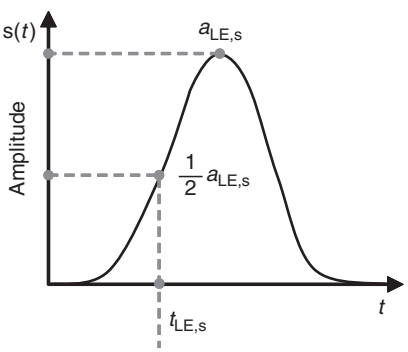

FIGURE 7.8
Attribute extraction with leading edge detection.

7.4.3 Constant Fraction Detection

A ranging implementation designed to be insensitive to amplitude-dependent biases applies a constant fraction detection circuit in which the pulse waveform $s(t)$ is inverted and delayed by a fixed time τ and added to the original pulse (Figure 7.9). The combined signal $s_{CFD}(t)$ gives a constant fraction signal with a zero crossing point at t_{CFD}.

$$s_{CFD}(t_{CFD}) = 0 \quad \text{with} \quad s_{CFD}(t) = s(t) - s(t+\tau) \tag{7.4}$$

The determined t_{CFD} is insensitive to the pulse amplitude, but depends on the pulse waveform and width (Kamermann, 1993). A suitable value for the delay time τ is the FWHM of the waveform.

For symmetric waveforms, the traditional constant fraction algorithm delivers unbiased ranging results. However, for an asymmetric noisy waveform the delayed signal should be reversed in time as well, to avoid ambiguities of the zero crossing point.

7.4.4 Center of Gravity Detection

The temporal center of gravity of the pulse waveform is ~~determined~~ (Figure ~~7.8d~~). The time value (range) is determined by integrating the pulse waveform $s(t)$

$$t_{CoG,s} = \int_{t=t_{CoG1,s}}^{t_{CoG2,s}} t\, s(t)\,\mathrm{d}t \Big/ \int_{t=t_{CoG1,s}}^{t_{CoG2,s}} s(t)\,\mathrm{d}t \tag{7.5}$$

It delivers good results for returns with various pulse amplitudes and pulse widths that have low noise. For returns with an asymmetric pulse shape skewed to longer ranges, this method results in a detected range that is slightly longer than the range value obtained with the peak detection.

The following methods to further process the pulse properties are not part of the center of gravity algorithm, but are well suited to complement it. Generally, integration over a section of the signal has the advantage of reducing the noise dependence compared to the

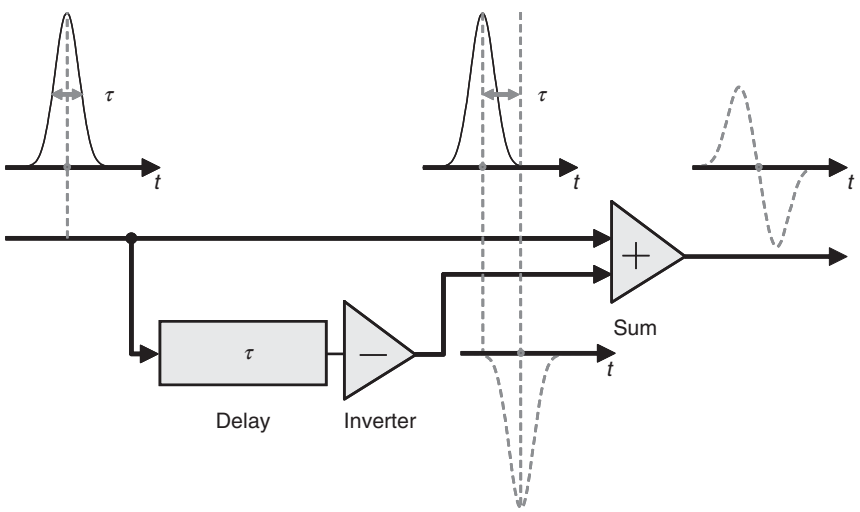

FIGURE 7.9
Simplified schematic visualization of the processing steps for the constant fraction detection.

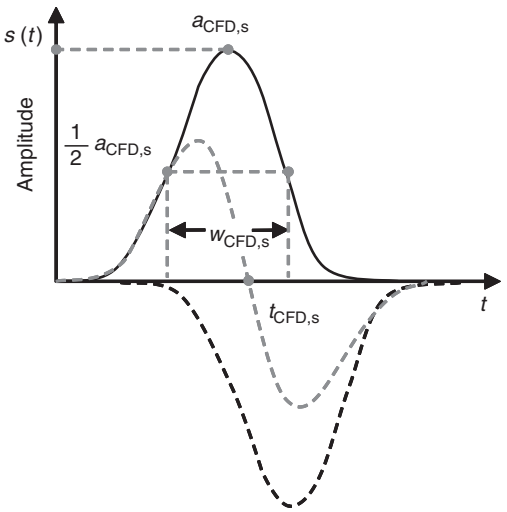

AQ4

FIGURE 7.10
Attribute extraction with constant fraction detection.

aforementioned methods relying on single samples. We call the integral of the waveform $s(t)$ shown in the denominator of Equation 7.4 as the pulse strength. From this, the value a_{CoG} can be calculated assuming a Gaussian and using the Inverse error function (erf^{-1}) and the width w

$$a_{CoG} = \frac{2\,\mathrm{erf}^{-1}(0.5)}{\sqrt{\pi}\,w} \int_{t=t_{CoG_1}}^{t_{CoG_2}} s(t)\,\mathrm{d}\,t \tag{7.6}$$

Furthermore, the width $W_{CoG,s}$ is approximated by the width of the central pulse area contributing 0.76 of this pulse strength with

$$\int_{t=t_{CoG}-\frac{w_0}{2}}^{t_{CoG}+\frac{w_0}{2}} s(t)\,\mathrm{d}\,t = \mathrm{erf}\left(\sqrt{\ln 2}\right) \int_{t=t_{CoG_1}}^{t_{CoG_2}} s(t)\,\mathrm{d}\,t \tag{7.7}$$

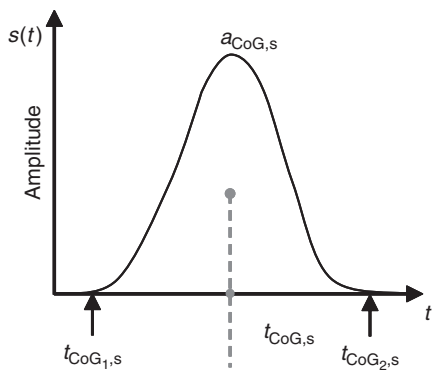

AQ4

FIGURE 7.11
Attribute extraction with center of gravity detection.

7.4.5 Gaussian Decomposition

Assuming a Gaussian function for the waveform (Equation 7.3), the surface attributes can be extracted by estimating the parameters of the adapted function:

$$s(t) = a_{\mathrm{GD,s}} \exp\left\{-4\ln(2)\frac{(t - t_{\mathrm{GD,s}})^2}{(w_{\mathrm{GD,s}})^2}\right\} \tag{7.8}$$

For a parametric description of the pulse properties, a Gaussian decomposition on the waveform can be used. Different methods are known, for example, Expectation Maximation (EM) algorithm (Persson et al., 2005) and Gauss–Newton or Levenberg–Marquardt algorithm (Hofton et al., 2000; Jutzi and Stilla, 2005; Reitberger et al., 2006). In Figure 7.12, the estimated attributes of the received waveform are depicted.

7.4.6 Deconvolution

Analysis of a received waveform in order to extract the attributes of the illuminated surface is a difficult task because different processes impact the shape of the waveform. The received waveform $s(t)$ of a laser pulse depends on the transmitted waveform $r(t)$, the impulse response of the receiver, the spatial beam distribution of the laser pulse, and the geometric and reflectance properties of the illuminated surface. The impulse response of the receiver is mainly affected by the photodiode and amplifier, and the spatial beam distribution typically has a Gaussian distribution. Let us assume that a receiver consists of an ideal photodiode and that the amplifier has an infinite bandwidth with a linear response. In that case the received waveform depends mainly on the transmitted waveform $r(t)$ and the properties of the illuminated surface. The 3d characteristics of the surface can be captured by a time-dependent surface representation, referred to as the surface response $h(t)$. In this case the received waveform $s(t)$ can be expressed as

$$s(t) = h(t) * r(t) \tag{7.9}$$

where $(*)$ denotes the convolution operation. By transforming $s(t)$ into the Fourier domain and solving the resulting equation for the spectral surface function $\underline{H}(f)$, we obtain

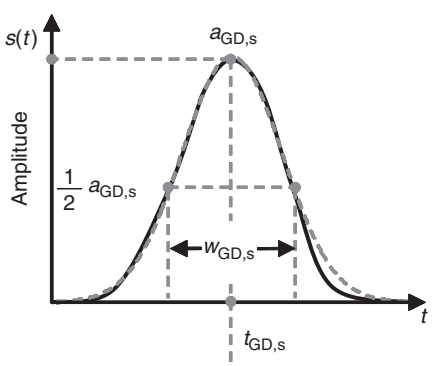

FIGURE 7.12
Attribute extraction with Gaussian decomposition algorithm.

$$\underline{H}(f) = \underline{S}(f)/\underline{R}(f) \tag{7.10}$$

The surface response $h(t)$ is obtained by transforming $\underline{H}(f)$ into the time domain. By applying a Gaussian decomposition method to the surface response, surface attributes can be extracted. The deconvolution removes the characteristics of the transmitted waveform from the received waveform and enables a description of the observed surface.

For a reliable deconvolution a high SNR for the received waveform is essential. In addition to this, the waveform has to be captured with a high bandwidth receiver and with an adequate sampling rate of the analog-to-digital converter. Furthermore, it has to be mentioned that large numerical errors may appear depending on the receiver noise. A Wiener filter used for deconvolution reduces the noise of the determined surface response (Jutzi and Stilla, 2006a). This method allows discriminating differences in range, e.g., given by a stepped surface within the beam, which are smaller than the length of the laser pulse. Experiments have shown that a step smaller than 10 times of the pulse length can be distinguished.

7.5 Attribute Extraction

An example of a signal profile applied to multiple pulses is depicted in Figure 7.13. The waveform parameters for each detected pulse of this signal profile are estimated by a Gaussian decomposition method using the Levenberg–Marquardt algorithm. The extracted attributes are described in the table. The estimated waveform is shown below the original waveform in Figure 7.13.

By comparing the range values in the table, we can observe that the distance between the first and second pulse is about 10 m and between the third and fourth pulse about 2.5 m.

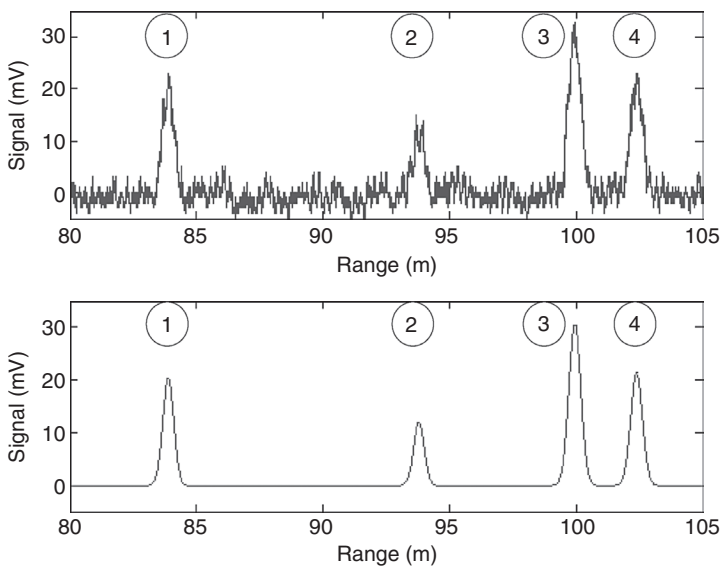

FIGURE 7.13
Signal profile with multiple reflections.

The third pulse shows the highest maximum amplitude and the pulse width of the first and second pulse is slightly lower than the third and fourth pulse. It is not possible to classify the type of surfaces illuminated within the single-beam corridor using the amplitude, pulse width, and range properties alone. For assigning each return pulse to a specific surface type additional information is required, which can result from the 3d geometrical relationships of the returns within a point cloud.

As an example of information retrieval achieved by combining return pulse properties and the spatial relationship of the returns, a full-waveform data set of a test scene was captured by scanning along the azimuth and elevation and recording the return intensity sampled over time t. Neglecting angular variations of the scan, the measured intensities as a function of time t sampled over the azimuth and elevation can be interpreted as a 3d data set forming a cuboid with Cartesian coordinates x, y, and t. The sampling along the time axis can be recalculated into corresponding range values z. These data cuboid can be analyzed in several different ways.

Figure 7.14 shows a set of image slices (y–t planes). The second slice from the left ($x = 4$) shows vegetation in the center (near range) and building structures on the right side (far range). The grey values correspond to the intensity of the signal. The intensity values along the marked solid line are the intensity values of the waveform shown in Figure 7.13.

Note that although this way of displaying the data suggests that a full 3d representation of the scene has been obtained, this is in fact not the case. Just as with point clouds measured by conventional laser scanners, the data cube represents only 2.5d information. This is because of occlusion effects that are dependent on the target size in relation to the beam footprint size. It is possible that the laser pulse is mostly intercepted by and backscattered from the first illuminated surface along the propagation direction and that the following surfaces along the laser vector are hidden, giving weak or no reflections. For instance, a tree with dense foliage may return only a single reflection response per laser pulse even though multiple surfaces are present after the first detected return along the path of the laser vector.

In the following, we use the Wiener filter method to extract attributes from received waveforms. The extraction is carried out without considering spatial neighborhood relations. The results of the extracted surface attributes from the data cuboid are shown in xy plane by

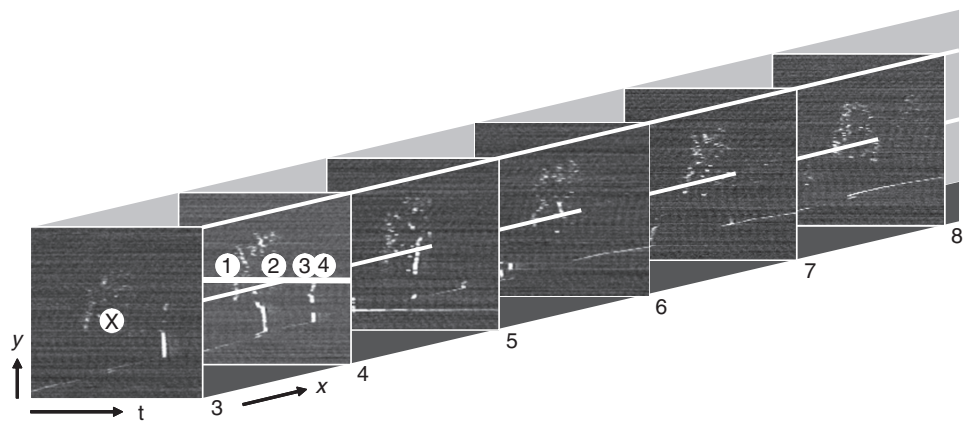

FIGURE 7.14
Vertical image slices with ground, vegetation, and building structures.

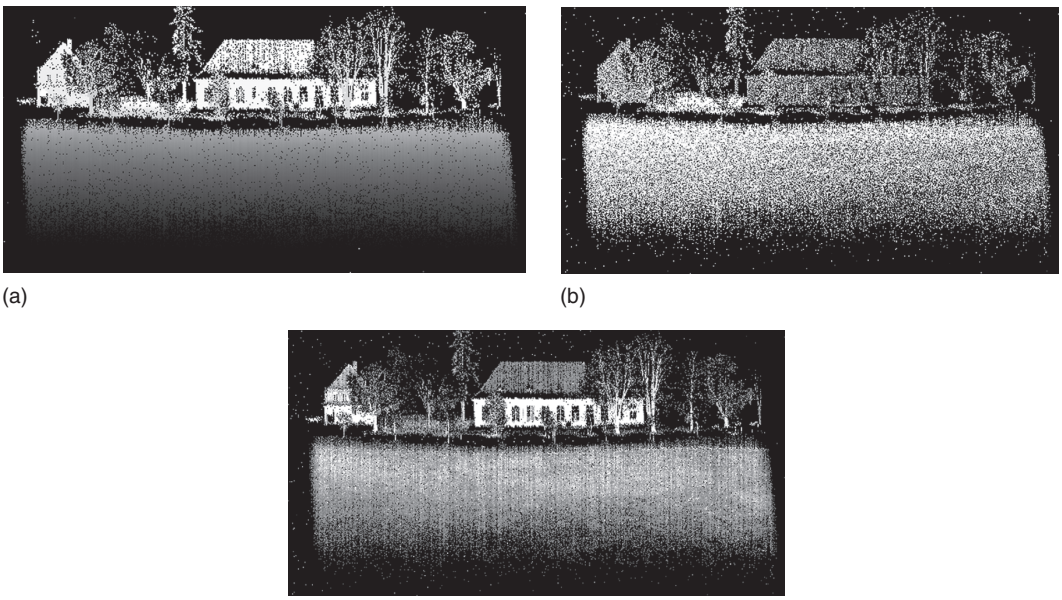

FIGURE 7.15
Extracted attributes of pulses: (a) range, (b) pulse width, and (c) intensity.

images of 320×600 pixels (Figure 7.15). Figure 7.15a shows the range image, Figure 7.15b shows the width of the pulse, and Figure 7.15c shows the intensity of the pulse. Larger values for an attribute are displayed by brighter pixels. Due to the fact that only a single value can be shown in the 2d images, only the first reflection is considered in cases where multiple reflections are present for a laser pulse.

The attributes maximum amplitude and pulse width were extracted using the Wiener filter and examined for their ability to discriminate different object classes. The entire scene and three objects classes, namely, buildings, trees, and meadow, are shown in Figure 7.16. Column A of the figure depicts range images of the entire scene (Figure 7.16a, column A) and of the selected objects classes (Figure 7.16b through d (column A)). Column B depicts scatter plots of maximum amplitude versus pulse width for the entire scene and the object classes (Figure 7.16, column B).

In Figure 7.16a, it can be observed that for the entire scene small values of the maximum amplitude have a large spreading of the pulse width. By decomposing the scene into the three object classes, it is apparent that the vegetation (trees and meadow) in most cases produces the signal returns with small maximum amplitudes but high values for the pulse width. The building in Figure 7.16b shows small values for the pulse width with little variation and a large range in the maximum amplitude values. Furthermore, the maximum amplitude of the building shows a cluster of higher values than that from the trees and meadow. These high values may result from high reflectance by the white façade. The trees are depicted in Figure 7.16c, where the pulse width shows high variation with mostly small maximum amplitude values. The meadow (Figure 7.16d) induces large variations of the pulse width and small maximum amplitude values. In general, the trees and the meadow produce larger pulse widths than the building.

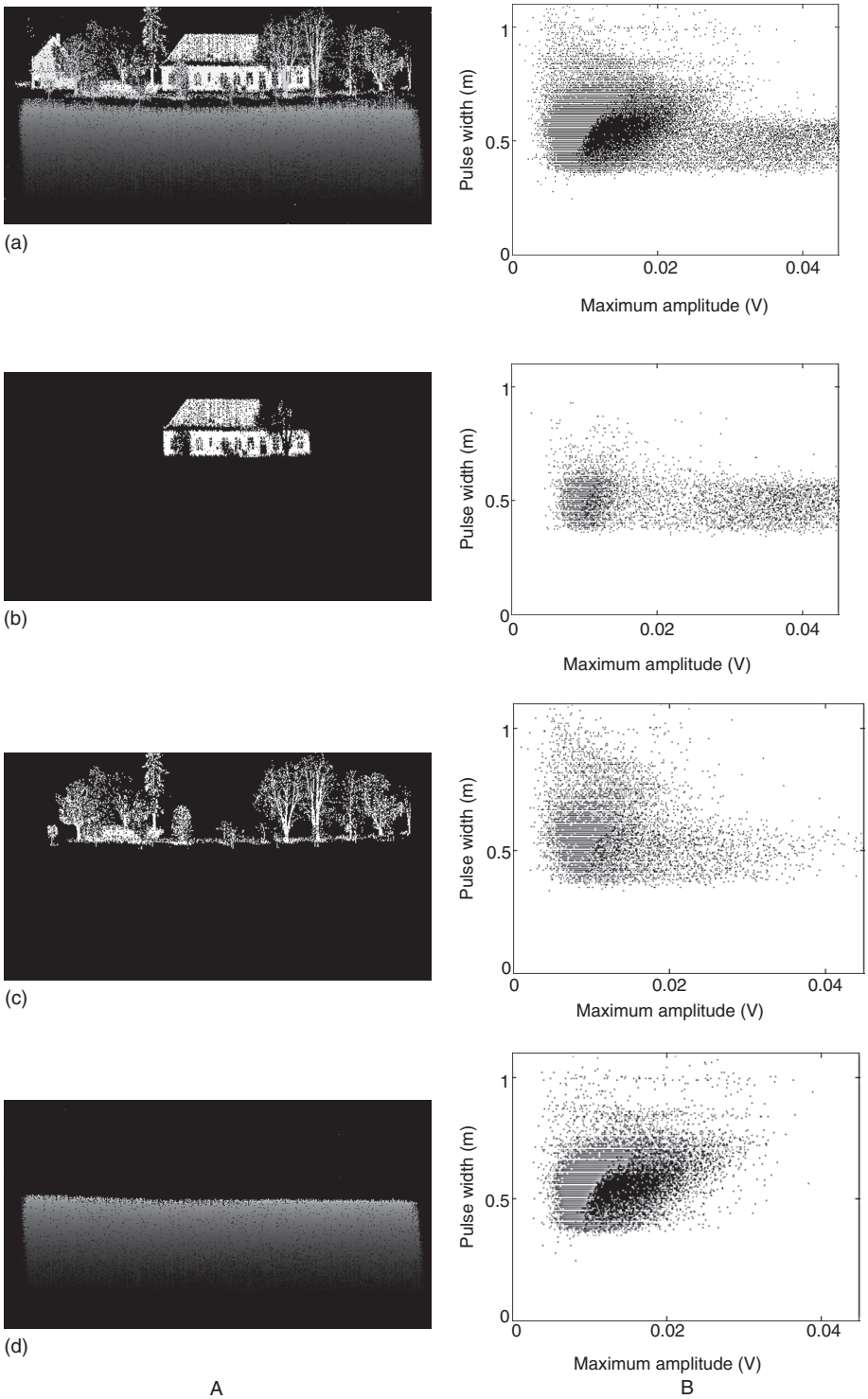

FIGURE 7.16
Comparison of maximum amplitude versus pulse width for selected objects of the measured scene. (a) Scene, (b) building, (c) trees, and (d) meadow. Column (A) denotes range images, and column (B) denotes maximum amplitude versus pulse width.

7.6 Summary and Outlook

It has been shown that full-waveform analysis enables extraction of more information compared to classical analogous pulse detection methods. First, recording of the received waveform offers the possibility for the end-user to select different methods to extract range information. The shape of the pulse and the entire signal can be considered for determining the range more accurately. Further improvements on reliability and accuracy can be derived by signal-processing methods based on the transmitted and the received waveform, e.g., deconvolution. Additionally, attributes of the surface can be derived from a parametric description of the waveform. The attributes maximum amplitude and pulse width may support the discrimination between volume scatterer (vegetation) and hard targets (man-made objects) (Kirchhof et al., 2007).

In the preceding description laser pulses were analyzed without considering the information of neighboring measurements. For reconstructing man-made objects, the introduction and test of hypotheses about the shape of the surface (e.g., plane, sphere) may efficiently support the analysis of single waveforms. Two different strategies assuming a planar shape in the local neighborhood of the surface and introducing this assumption into the signal analysis should be addressed. Both strategies combine information from top-down (surface primitives) and bottom-up (signal processing) for an extended analysis of full waveform laser data.

The first strategy (Kirchhof et al., 2007) uses an iterative processing of waveforms considering a predicted shape of the waveform from the local neighborhood. A presegmentation based on surface attributes is carried out to distinguish between partly penetrable objects (e.g., trees, bushes) and impenetrable surfaces (e.g., roof, wall). Derived range values from presegmentation of the impenetrable surfaces are used to automatically generate surface primitives (e.g., planes).

This allows a refinement of each range value, considering the surface geometry in a close neighborhood. Furthermore, partly occluded surface areas are extended by prediction of the expected range values. This prediction is further improved by considering the surface slope for the estimated received waveform. Expected pulses are simulated and correlated with the received waveforms. Accepted points that were missed in the first processing step due to weak signal response are associated to the point cloud. The procedure is repeated several times until all appropriate range values are considered to estimate the surface.

The second strategy (Stilla et al., 2007) uses a slope compensated stacking of waveforms. Weak pulses with a low SNR are discarded by classic threshold methods and get lost. In signal and image processing, different stacking techniques are used to improve the SNR.

For detection of weak laser pulses, hypotheses for planes of different slopes (e.g., angle difference 5°) are generated. According to the slope of the hypothesis, the waveforms in the local neighborhood are shifted in range. A superimposed signal is calculated from the stack of shifted waveforms. The maxima of superimposed signals from all hypotheses are compared to verify a hypothesis. Each signal is assessed by a likelihood value with respect to its contribution to the accepted hypothesis. Finally, signals are classified according to the λ-values obtained using two thresholds and visualized by the traffic-light paradigm. The results contain detected pulses reflected from objects, which cannot be predicted by the previously detected point cloud. AQ5

Both strategies show promising results that encourage the continuity of work on the analysis of full-waveform laser pulses.

References

Abshire, J.B., Sun, X.L., Riris, H., Sirota, J.M., McGarry, J.F., Palm, S., Yi, D.H., and Liiva, P., 2005. Geoscience Laser Altimeter System (GLAS) on the ICESat mission: On-orbit measurement performance. *Geophysical Research Letters*, 32:L21S02, doi:10.1029/2005GL024028.

Albertz, J., Attwenger, M., Barrett, J., Casley, S., Dorninger, P., Dorrer, E., Ebner, H., Gehrke, S., Giese, B,. Gwinner, K., Heipke, C., Howington-Kraus, E., Kirk, R.L., Lehmann, H., Mayer, H., Muller, J.-P., Oberst, J., Ostrovskiy, A., Renter, J., Reznik, S., Schmidt, R., Scholten, F., Spiegel, M., Stilla, U., Waehlisch, M., and Neukum, G., 2005. HRSC on Mars Express—Photogrammetric and Cartographic Research. *Photogrammetric Engineering and Remote Sensing*, 71(10):1153–1166.

Alexander, S.B., 1997. Optical communication receiver design. In: *SPIE Tutorial Texts in Optical Engineering*, TT22, SPIE Press, Bellingham, WA.

Blair, J.B., Rabine, D.L., and Hofton, M.A., 1999. The Laser Vegetation Imaging Sensor (LVIS): A medium-altitude, digitization-only, Airborne Laser Altimeter for mapping vegetation and topography. *ISPRS Journal of Photogrammetry and Remote Sensing*, 54(2–3):112–122.

Brenner, A.C., Zwally, H.J., Bentley, C.R., Csatho, B.M., Harding, D.J., Hofton, M.A., Minster, J.B., Roberts, L.A., Saba, J.L., Thomas, R.H., and Yi, D., 2003. Geoscience Laser Altimeter System (GLAS)—Derivation of range and range distributions from Laser Pulse Waveform Analysis for surface elevations, roughness, slope, and vegetation heights. Algorithm Theoretical Basis Document—Version 4.1. Available at http://www.csr.utexas.edu/glas/pdf/Atbd_20031224.pdf (accessed September 1, 2006).

Gagliardi, R.M. and Karp, S., 1976. *Noncoherent (Direct) Detection: Optical Communications*. John Wiley & Sons, New York.

Harding, D.J. and Carabajal, C.C., 2005. ICESat waveform measurements of within-footprint topographic relief and vegetation vertical structure. *Geophysical Research Letters*, 32:L21S10, doi:10.1029/2005GL023471.

~~Hecht, J., 1992. *The Laser Guidebook*, 2nd ed., Tab Books, Blue Ridge Summit, PA.~~ AQ6

~~Hofton, M.A. and Blair, J.B., 2002. Laser altimeter return pulse correlation: A method for detecting surface topographic change. *Journal of Geodynamics* 34(3):477–489.~~ AQ7

Hofton, M.A., Minster, J.B., and Blair, J.B., 2000. Decomposition of laser altimeter waveforms. *IEEE Transactions on Geoscience and Remote Sensing*, 38(4):1989–1996.

Irish, J.L. and Lillycrop, W.J., 1999. Scanning laser mapping of the coastal zone: The SHOALS System. *ISPRS Journal of Photogrammetry and Remote Sensing*, 54(2–3):123–129.

Jelalian, A.W., 1992. *Laser Radar Systems*. Artech House, Boston, MA.

Jutzi, B. and Stilla, U., 2005. Measuring and processing the waveform of laser pulses. In: Gruen, A., Kahmen, H., Eds., *Optical 3-D Measurement Techniques VII*, Vol. 1, pp. 194–203. AQ8

Jutzi, B. and Stilla, U., 2006a. Range determination with waveform recording laser systems using a Wiener filter. *ISPRS Journal of Photogrammetry and Remote Sensing*, 61(2):95–107 [doi:10.1016/j.isprsjprs.2006.09.001].

Jutzi, B. and Stilla, U., 2006b. Characteristics of the measurement unit of a full-waveform laser system. Symposium of ISPRS Commission I: From Sensors to Imagery. *International Archives of Photogrammetry, Remote Sensing and Spatial Information Sciences*, 36(Part 1/A).

Kamermann, G.W., 1993. Laser radar. In: Fox, C. S., Ed., *Active Electro-Optical Systems, The Infrared and Electro-Optical Systems Handbook*. SPIE Optical Engineering Press, Ann Arbor, MI.

Kirchhof, M., Jutzi, B., and Stilla, U., 2007. Iterative processing of laser scanning data by full waveform analysis, *ISPRS Journal of Photogrammetry and Remote Sensing* (in press) [doi:10.1016/j.isprsjprs.2007.08.006]. AQ9

Lenhart, D., Kager, H., Eder, K., Hinz, S., and Stilla, U., 2006. Hochgenaue Generierung des DGM vom vergletscherten Hochgebirge—Potential von Airborne Laserscanning. Arbeitsgruppe Automation in der Kartographie: Tagung 2005, Mitteilungen des Bundesamtes für Kartographie und Geodaesie, Band 36:65–78 (in German). AQ10

Loudon, R., 1973. *The Quantum Theory of Light*. Clarendon Press, Oxford.

Papoulis, A., 1984. *Probability, Random Variables, and Stochastic Processes*. McGraw-Hill, Tokyo.

Persson, Å., Söderman, U., Töpel, J., and Ahlberg, S., 2005. Visualization and analysis of full-waveform airborne laser scanner data. In: Vosselman, G., Brenner, C., Eds., *Laserscanning 2005. International Archives of Photogrammetry, Remote Sensing and Spatial Information Sciences*, 36(Part 3/W19):109–114.

Reitberger, J., Krzystek, P., and Stilla, U., 2006. Analysis of full waveform lidar data for tree species classification. In: Förstner, W., Steffen, R., Eds., Symposium of ISPRS Commission III: Photogrammetric Computer Vision PCV06. *International Archives of Photogrammetry, Remote Sensing and Spatial Information Sciences*, 36(Part 3):228–233.

Reitberger, J., Krzystek, P., and Stilla, U., 2007. Analysis of full waveform LIDAR data for the classification of deciduous and coniferous trees. *International Journal of Remote Sensing* (in press). AQ11

Schutz, B.E., Zwally, H.J., Shuman, C.A., Hancock, D., and DiMarzio, J.P., 2005. Overview of the ICESat Mission. *Geophysical Research Letters*, 32, L21S01, [doi:10.1029/2005GL024009].

Spiegel, M., Stilla, U., and Neukum, G., 2006. Improving the exterior orientation of Mars Express regarding different imaging cases. *International Archives of Photogrammetry and Remote Sensing and Spatial Information Sciences*, 36(4) (on CD). AQ12

Stilla, U., Yao, W., and Jutzi, B., 2007. Detection of weak laser pulses by full waveform stacking. In: Stilla, U. et al., Eds., PIA07: Photogrammetric Image Anlysis 2007. *International Archives of Photogrammetry, Remote Sensing and Spatial Information Sciences*, 36(3/W49A):25–30.

Steinvall, O., 2000. Effects of target shape and reflection on laser radar cross sections. *Applied Optics*, 39(24):4381–4391.

Thiel, K.H. and Wehr, A., 2004. Performance capabilities of laser-scanners—An overview and measurement principle analysis. *International Archives of Photogrammetry, Remote Sensing and Spatial Information Sciences*, 36(Part 8/W2):14–18.

Troup, G.J., 1972. Photon Counting and Photon Statistics. In: Sanders, J.H., Stenholm, S., Eds., *Progress in Quantum Electronics*, Vol. 2 (Part 1), Oxford, Pergamon.

Wagner, W., Ullrich, A., Ducic, V., Melzer, T., and Studnicka, N., 2006. Gaussian decomposition and calibration of a novel small-footprint full-waveform digitising airborne laser scanner. *ISPRS Journal of Photogrammetry and Remote Sensing*, 60(2):100–112.

Wuerlaender, R., Eder, K., and Geist, T., 2004. High quality DEMs for glacier monitoring: Image matching versus laser scanning. In: Altan, M.O., Ed., *International Archives of Photogrammetry and Remote Sensing*, 35(Part B7):753–758.

Zwally, H.J., Schutz, B., Abdalati, W., Abshire, J., Bentley, C., Brenner, A., Bufton, J., Dezio, J., Hancock, D., Harding, D., Herring, T., Minster, B., Quinn, K., Palm, S., Spinhirne, J., and Thomas, R., 2002. ICESat's Laser Measurements of polar ice, atmosphere, ocean, and land. *Journal of Geodynamics*, 34(3–4):405–445.

AUTHOR QUERIES

[AQ1] Please add "Harding et al., 2005" to the list.
[AQ2] Please check whether edit to the sentence: "In this chapter.….principles." is ok.
[AQ3] Please confirm whether "AM" refers to "amplitude modulation" or "amplitude modulated".
[AQ4] Please provide citation for Figures 7.10 and 7.11.
[AQ5] Please advise whether the intended meaning has been retained in this sentence.
[AQ6] Please provide citation for reference "Hecht, 1992."
[AQ7] Please provide citation for reference "Hofton and Blair, 2002"
[AQ8] Please update reference with publisher details.
[AQ9] Please update reference with year, volume number and page range.
[AQ10] Please provide citation for reference "Lenhart et al., 2006."
[AQ11] Please update reference with year of publishing and other missing details.
[AQ12] Please confirm the edit made in this reference.